arXiv:1607.02853v1 [cond-mat.supr-con] 11 Jul 2016

Orbital-dependent charge dynamics in MnP revealed by optical study

P. Zheng,[1,*] Y. J. Xu,[1] W. Wu,[1] G. Xu,[1] J. L. Lv,[1] F. K. Lin,[1] P. Wang,[1] Yi-feng Yang,[1,2,†] and J. L. Luo[1,2]

[1]*Beijing National Laboratory for Condensed Matter Physics, Institute of Physics, Chinese Academy of Sciences, Beijing 100190, P. R. China*

[2]*Collaborative Innovation Center of Quantum Matter, Beijing 100190, China*

(Dated: July 12, 2016)

The orthorhombic structure MnP is a newly discovered superconductor under $7-8\,$GPa at the boarder of a helimagnetic phase. We present for the first time the optical conductivity study of high quality MnP single crystals at different temperatures crossing the para-ferromagnetic and ferro-helimagnetic transitions at ambient pressure. Our data reveals two types of charge carriers with very different lifetimes. In combination with the first-principles calculations, we show that the short lifetime carriers are quasi-one-dimensional and become gapped in the helimagnetic phase, causing a dramatic change in the low-frequency optical spectra, whereas the long lifetime carriers are strongly anisotropic three-dimensional like which are little affected by the magnetic phase transitions and provide major contributions to the transport properties. This orbital-dependent charge dynamics originates from the special crystal structure of MnP and may be extended to high pressures, providing a basis for our understanding of the unconventional superconductivity and its interplay with helimagnetism.

PACS numbers: 74.25.Gz, 78.20.-e, 78.30.-j

The discoveries of superconductivity in the helical magnets CrAs [1, 2] and MnP [3] reveal a fascinating new family of superconductivity emerging at the boarder of long-range helimagnetic orders. As the first manganese-based superconductor, MnP has a helimagnetic ground state at ambient pressure. Gradually applying pressure on good single crystals first destroys the helimagnetic order at about 1.2 GPa and then yields a second helimagnetic phase at higher pressures as revealed very recently by synchrotron-based magnetic X-ray diffraction techniques, neutron diffraction, muon-spin rotation and nuclear magnetic resonance (NMR) [4–9]. Near the critical pressure of 7.8 GPa, where the second helimagnetic phase is also suppressed, superconductivity emerges with $T_c \approx 1\,$K. Above T_c, the resistivity exhibits non-Fermi liquid behavior and reveals a dramatic enhancement of the quasiparticle effective mass at low temperatures in the normal state, suggesting an unconventional pairing mechanism for the observed superconductivity at the border of the helimagnetic phase [3]. Understanding the relation between superconductivity and helimagnetism is the major issue in this material.

To shed light on the nature of the charge dynamics and its interplay with magnetism, we performed infrared optical measurements on MnP at temperatures from 300 K to 10 K at ambient pressure, where a para-ferromagnetic transition has been reported at about $T_{C1} = 289.5 - 292\,$K and a ferro-helimagnetic transition at $T_{C2} = 47 - 53\,$K in previous studies [3, 10–17]. In the helimagnetic state, the Mn spins rotate within the ab plane with a propagation vector Q_h along the c-axis [12]. The compound remains metallic at all temperatures and no structural change has been reported with temperature. The temperature dependent optical investigation hence allows us to reveal the behavior of the charge carriers in response to the complicated magnetic orders, which, to the best of our knowledge, has not been done previously. We find for the first time that the low-frequency metallic responses in the ferromagnetic phase can be best understood as a sum of two Drude components, one of which has a very short lifetime and becomes gapped in the helimagnetic phase, causing a dramatic change in the low-frequency optical spectra crossing the ferro-helimagnetic phase transition. This indicates two types of charge carriers with very different lifetimes. In combination with the first-principles calculations, we identify that the short lifetime carriers are quasi-one-dimensional (1D) like along the Mn chains (b-axis) and contribute mostly to the magnetic properties, whereas the long lifetime carriers have quasi-two-dimensional (2D) or strongly anisotropic three-dimensional (3D) Fermi surfaces and are largely responsible for the transport properties such as the dc conductivity. Our results reveal an orbital-dependent helimagnetic phase transition and suggest a microscopic two-fluid picture for the charge dynamics in MnP, which puts a constraint on any serious microscopic model and may be taken as a basis for our understanding of the interplay between unconventional superconductivity and helimagnetism at high pressures.

Four needle-shaped single crystals, three with an average size of about $2 \times 0.3 \times 0.08\,\mathrm{mm}^3$ and one about $2.1 \times 1.4 \times 0.5\,\mathrm{mm}^3$, have been grown using selenium-flux method and used in this experiment [3]. The dc resistivity ρ_{dc} and the specific heat C_p were measured with the four-probes method and the thermal relaxation method, respectively, in a quantum design physical property measurement system (PPMS). Fig. 1(a) shows a typical result of the dc conductivity $\sigma_{dc}(T) = 1/\rho_{dc}(T)$ along the b-axis. We see that the compound remains

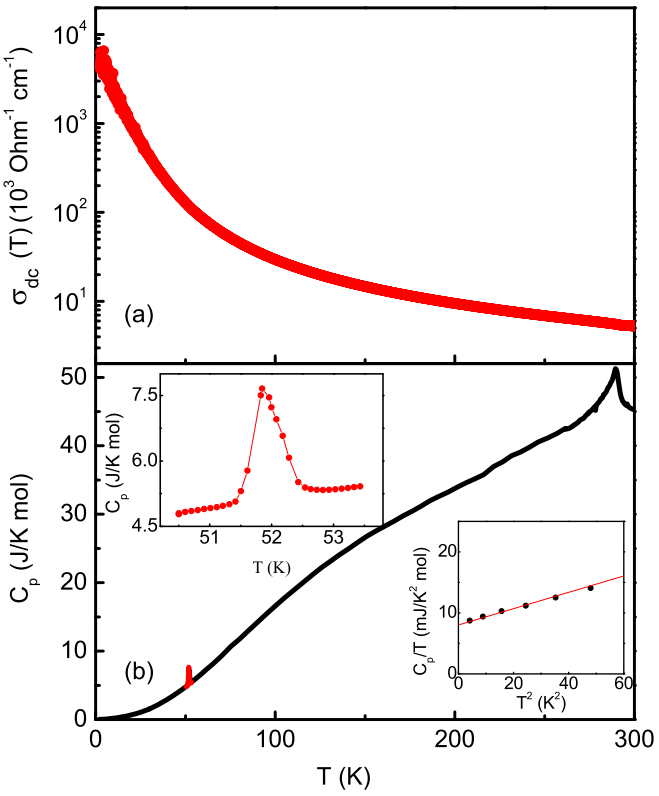

FIG. 1: (Color online) (a) The *dc* conductivity σ_{dc}(T) measured along the *b*-axis as a function of temperature; (b) The specific heat $C_p(T)$ as a function of temperature, showing a para-ferromagnetic transition at about 290 K and a ferro-helimagnetic transition at about 51.8 K. The insets show the specific heat peak at the ferro-helimagnetic phase transition in the enlarged scale and the fit of $C_p(T)/T$ versus T^2 at low temperatures.

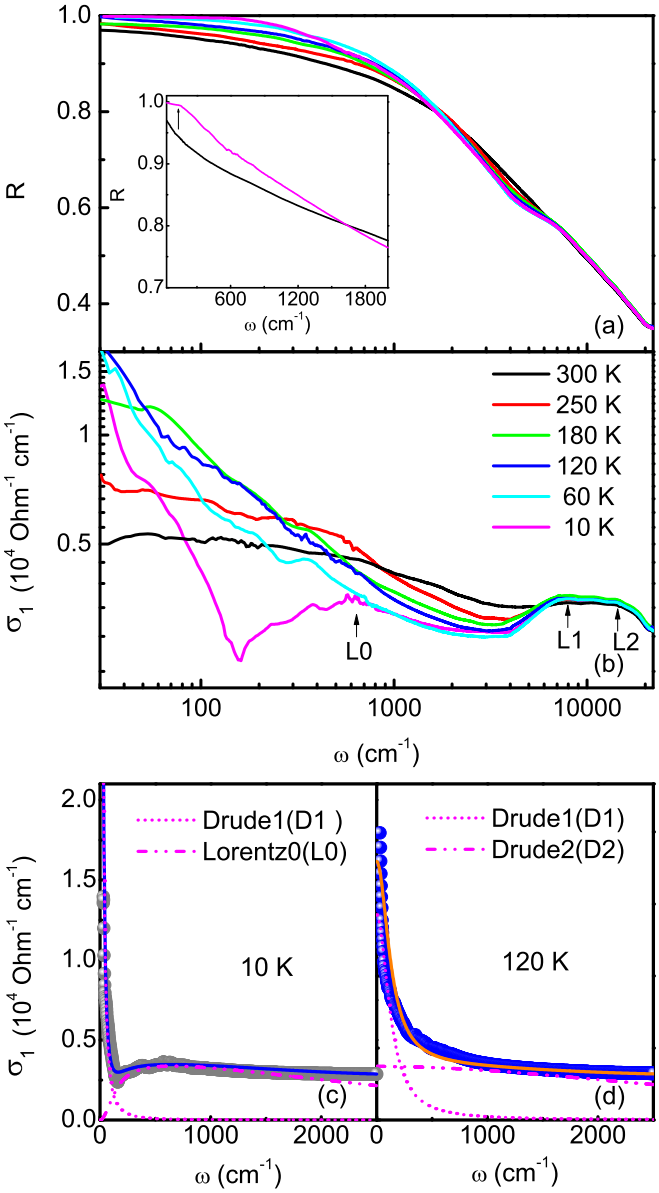

FIG. 2: (Color online) (a) Variation of the reflectivity spectra $R(\omega)$ with temperature. The black arrow in the inset denotes the low-ω reflectance edge at 10 K. (b) Variation of the real part of the optical conductivity spectra with temperature. The two peaks centered at high frequencies remain almost unchanged with temperature. (c) Multi-component fit to the optical conductivity at 120 K and 10 K, showing the contributions of the two low-frequency components.

metallic at all temperatures and our sample has a very high RRR ratio, $\sigma_{dc}(2\,\mathrm{K})/\sigma_{dc}(300\,\mathrm{K}) \approx 1000$, similar to that of the superconducting sample [3]. The temperature dependence of the specific heat is plotted in Fig. 1(b). A para-ferromagnetic transition and a ferro-helimagnetic transition are observed at about 290 K and 51.8 K, respectively. As shown in the inset, a tiny sharp peak is seen for the first time at the ferro-helimagnetic phase transition, owing to the high quality of our single crystals [18, 19]. At low temperatures, the specific heat can be nicely fit with $C_p/T = \gamma_e + \beta T^2$, where $\gamma_e \approx 8.3\,\mathrm{mJ/mol\ K^2}$ is the residual electron specific heat coefficient and the βT^2 term is the phonon contribution. Interestingly, neither the conductivity nor the specific heat seems to be much affected by the helimagnetic phase transition.

The optical reflectivity $R(\omega)$ was measured from 30 cm^{-1} to 25000 cm^{-1} at different temperatures on the Fourier transform spectrometers (Bruker 113 v and 80 v/s) using an *in situ* gold and aluminium overcoating technique. The frequency-dependent optical conductivity $\sigma(\omega)$ was derived from the Kramers-Kronig transformation using the Hagen-Rubens relation for the low-frequency extrapolation. In the high frequency region, the reflectivity was extrapolated as a constant to $\omega = 80000\,\mathrm{cm}^{-1}$, above which a well-known function of ω^{-4} was used. Fig. 2(a) plots the measured reflectivity spectra $R(\omega)$ at various temperatures. It is seen that as temperature decreases, $R(\omega)$ increases in the low frequency region, but decreases at higher frequency region below $8000\,\mathrm{cm}^{-1}$. All the spectra intersect be-

tween 1000 cm^{-1} and 2000 cm^{-1}. At low temperatures, a broad peak emerges at about 8000 cm^{-1}, above which all spectra merge together and decrease monotonically with increasing ω, whereas the low-frequency reflectivity, as shown in the inset of Fig. 2(a), increases faster towards unity than those at higher temperatures, giving rise to a low-ω reflectance edge at 10 K in the optical conductivity.

The above features are more pronounced in the real part of the optical conductivity, $\sigma_1(\omega)$, as plotted in Fig. 2(b) for a variety of temperatures ranging from 10 K to 300 K. Two broad peaks are seen centered at about 8100 cm^{-1} and 16000 cm^{-1}, independent of temperature. These peaks may be attributed to electronic correlations or inter-band transitions between the bonding/antibonding bands of Mn-3d and P-3p orbitals [20–22]. For intermediate frequencies between 1500 cm^{-1} and 5000 cm^{-1}, the spectra depend weakly on frequency and decrease gradually with lowering temperature. In the low frequency region, on the other hand, a peak is seen to grow gradually from 300 K to 60 K and then, quite unexpectedly, split into a very narrow peak below about 100 cm^{-1} and a broad peak centered at about 650 cm^{-1}, with a dip at about 180 cm^{-1} where the optical conductivity is strongly suppressed in resemblance of those from the spin density wave gap in pnictides and the hybridization gap in heavy fermion materials. We note that this sudden splitting of the low-frequency peak is accompanied with the ferro-helimagnetic transition at about 51.8 K and has not been observed in previous studies.

To explore the temperature evolution of the charge carriers, we analyze $\sigma_1(\omega)$ using a combined multi-component Drude and Lorentz formula,

$$\sigma_1(\omega) = \sum_i \frac{\omega_{p,i}^2}{4\pi} \frac{\gamma_i}{\omega^2 + \gamma_i^2} + \sum_j \frac{\Omega_j^2}{4\pi} \frac{\omega^2 \Gamma_j}{(\omega^2 - \omega_{0,j}^2)^2 + \Gamma_j^2 \omega^2},$$

where the first term gives the Drude contribution from itinerant charge carriers with the plasma frequencies $\omega_{p,i}$ and the scattering rates γ_i, and the second Lorentz term originates typically from inter-band transitions located at $\omega_{0,j}$ (corresponding to the direct gap) with the strength Ω_j and the damping coefficient Γ_j. Fig. 2(c) shows two typical examples of our fit for the optical spectra at 120 K in the ferromagnetic phase and 10 K in the helimagnetic phase. We find that at least four components are needed in order to obtain a good fit to the experimental data. In addition to the two Lorentz components describing the peaks centered at $\omega_{0,1} \approx 8100\,\mathrm{cm}^{-1}$ and $\omega_{0,2} \approx 16000\,\mathrm{cm}^{-1}$ (denoted as L1 and L2), two Drude components (denoted as D1 and D2) are required to fit the low and intermediate frequency regions in the ferromagnetic phase, and one Drude component (D1) and one Lorentz component (L0) in the helimagnetic phase. This indicates that there exist at least two types of charge carriers that behave very differently across the ferro-helimagnetic phase transition in MnP.

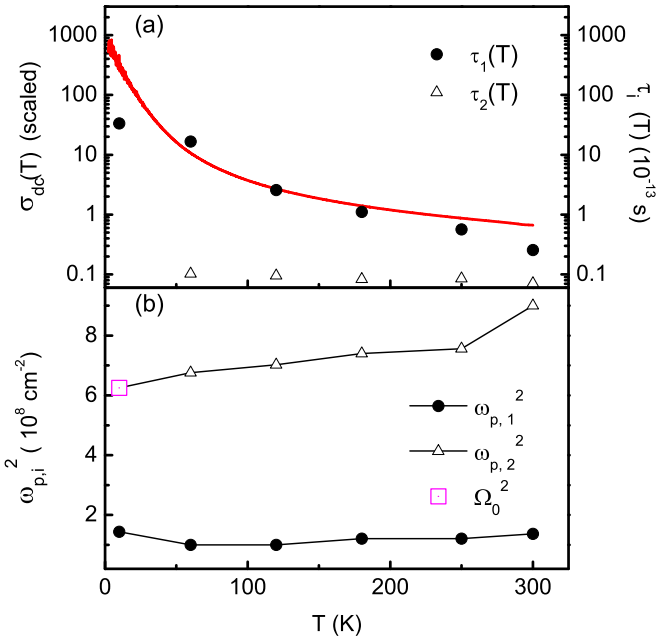

FIG. 3: (Color online) (a) Temperature dependence of τ_i and its comparison with the scaled dc conductivity (solid line). (b) Temperature dependence of $\omega_{p,i}^2$ in the ferromagnetic phase and its comparison with Ω_0^2 at 10 K in the helimagnetic phase.

The fitting parameters are listed in Table I for all measured temperatures. Fig. 3 compares the derived parameters as a function of temperature for the two low-frequency components. We see that the two types of carriers have very different lifetimes calculated using $\tau_i = 1/\gamma_i$. One has a long lifetime (τ_1) increasing from 2.6×10^{-14} s to 3.0×10^{-12} s as temperature decreases from 300 K to 10 K, and the other has a much shorter lifetime (τ_2) of the order of 7×10^{-15} s that remains almost temperature independent. A simple comparison with other materials suggests that the former (τ_1) behaves like a good metal ($\tau > 10^{-13}$ s) at low temperatures, whereas the latter (τ_2) is strongly damped. As already shown in Fig. 2(c), the low-frequency conductivity is dominated by the long lifetime carriers already at 120 K. This is further supported by the overall agreement between the scaled dc conductivity and τ_1 in Fig. 3(a). The relative contribution of the short lifetime carriers to the conductivity becomes significantly less important as τ_2/τ_1 decreases rapidly with lowering temperature. Fig. 3(b) compares the plasma frequencies of both carriers. We see that $\omega_{p,1}^2$ changes only slightly as the temperature crosses the magnetic transitions, whereas $\omega_{p,2}^2$ shows a larger change across the para-ferromagnetic transition and seems to be more related to the magnetic properties. Moreover, the strength Ω_0^2 of the low-frequency Lorentz component (L0) at 10 K is very close to the value of $\omega_{p,2}^2$ of the second Drude term (D2) at 60 K. Since these two

TABLE I: The fitting parameters at 300 K, 250 K, 180 K, 120 K,60 K, and 10 K.

T (K)	D1 (cm^{-1})		D2/L0 (cm^{-1})			L1 (cm^{-1})			L2 (cm^{-1})		
	$\omega_{p,1}$	γ_1	-	$\omega_{p,2}$	γ_2	$\omega_{0,1}$	Ω_1	Γ_1	$\omega_{0,2}$	Ω_2	Γ_2
300	11700	1300	-	30000	4700	8100	43500	15000	16000	37400	13900
250	11000	590	-	27500	3900	8100	45000	13700	16000	37400	13900
180	11000	300	-	27200	4000	8100	45500	13700	16000	37400	13900
120	10000	130	-	26500	3500	8100	45000	13000	16000	37400	13900
60	10000	20	-	26000	3250	8100	45500	13000	16000	37400	13900
T (K)	$\omega_{p,1}$	γ_1	$\omega_{0,0}$	Ω_0	Γ_0	$\omega_{0,1}$	Ω_1	Γ_1	$\omega_{0,2}$	Ω_2	Γ_2
10	12000	10	650	25000	3100	8100	47500	13900	16000	37400	13900

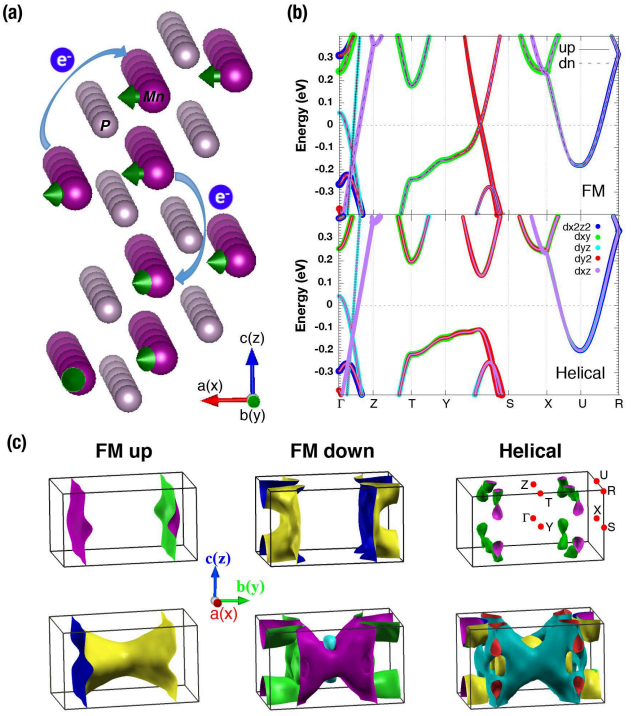

FIG. 4: (Color online) (a) Illustration of the crystal structure and the helimagnetic order. (b) Comparison of the band structures in the ferromagnetic and helimagnetic states. (c) Comparison of the Fermi surfaces for the ferromagnetic and helimagnetic states, showing the suppression of the quasi-1D Fermi sheets in the helimagnetic state.

quantities represent respectively the total spectral weight of the corresponding Drude or Lorentz terms, their equality indicates that they originate from the same carriers, namely the short lifetime carriers that become gapped in the helimagnetic phase, turning the broad Drude peak into a Lorentz form in the optical spectra. We hence conclude that there exist two distinct types of charge carriers in MnP which behave very differently and govern the transport (long lifetime carriers) and magnetic (short lifetime carriers) properties, respectively.

To understand the microscopic origin of both carriers, we performed the first-principles calculations for MnP using the full-potential augmented plane-wave and local orbital methods, as implemented in the WIEN2k code [23] and the non-collinear WIENNCM code [24]. The Perdew-Burke-Ernzerhof generalized gradient approximation (GGA) was used for the exchange-correlation functional in both codes. The material belongs to the space group $Pnma$ with an orthorhombic crystal structure and the lattice parameters are taken as $a = 5.26$ Å, $b = 3.17$ Å and $c = 5.92$ Å from previous work [25]. For the ferromagnetic state, we obtain similar results with both codes, providing a consistency check for our numerical calculations. The helimagnetic state was calculated with the propagation vector $Q_h = (0, 0, 0.117)$ as observed in experiment [12]. The derived specific heat is about 4.4 mJ/mol K^2, close to the experimental value of $\gamma_e \approx 8.3$ mJ/mol K^2, indicating weak electronic correlations and providing a further justification of our GGA calculations.

Fig. 4 shows the resulting band structures and Fermi surfaces for both the ferromagnetic and helimagnetic states in the unfolded Brillouin zone. In the ferromagnetic phase, the major Fermi surfaces have an interesting topology and are composed of one flat sheet and one sheet of the cylindric shape for each spin component. Both flat sheets show weak dispersion within the xz plane and originate from the two intersecting bands along the Y-S direction in the Brillouin zone as shown in Fig. 4(b). They are formed mainly by the Mn d_{y^2}-orbital that extends along the one-dimensional Mn chain, namely the b-axis, as illustrated in Fig. 4(a). The two cylindric Fermi surfaces contain other Mn d-orbitals and exhibit quasi-2D or strongly anisotropic 3D character. The band structures of the helimagnetic phase show little changes except along the Y-S direction, where the two intersecting bands hybridize and open a small gap, owing to the helimagnetism that causes a mixture of the two spin components in neighboring Mn chains. In the optical measurement, this suppresses part of the optical spectra and gives rise to the dip feature as seen in Fig. 2(b), in resemblance of those from the spin density wave gap in pnictides and the hybridization gap in heavy fermion materials. As a

consequence, the Fermi surfaces show dramatic changes in the helimagnetic phase. The two flat sheets disappear completely, leaving a number of small pockets spreading at the corners of the Brillouin zone. These small pockets would be suppressed if the Coulomb interaction is taken into account. The cylindrical Fermi surfaces are also modified and become more 3D like. Our results are in exact correspondence with the optical analysis and indicate that the short lifetime carriers originate from the d_{y^2}-orbital along the b-axis showing quasi-1D character and the long lifetime carriers contain the contributions from other Mn d-orbitals.

We note that the existence of two types of charge carriers with distinct properties results naturally from the particular crystal structure of MnP and is therefore robust against pressure or other external tuning parameters without altering the crystal structure [26]. The fact that the two types of carriers dominate separately the transport and magnetic properties provides a possible simplification for our understanding of its exotic and complicated physics [3, 10]. For example, the heilmagnetic order may be attributed to the exchange interaction between neighboring Mn spin chains formed mainly by the d_{y^2} orbitals and the Fermi liquid behavior in the helimagnetic phase at ambient pressure may be largely attributed to the long lifetime carriers from all other orbitals. At the helimagnetic transition, the small dip in the c-axis resistivity could be understood from the magnetic scattering of the long lifetime carriers by the helimagnetic fluctuations in the xz-plane, whereas no clear signature is observed in the resistivity along the b-axis which remains ferromagnetically ordered. Our results also put a strict constraint on any serious theoretical investigations. A proper microscopic model should contain at least two bands of different characters and treat correctly the quasi-1D nature of the Mn $3d_{y^2}$-orbitals. Taking this as a starting point, we speculate that at higher pressures, the superconducting and helimagnetic properties of MnP may also be attributed to the interplay between the two types of carriers, causing non-Fermi liquid behavior and pairing condensation near the helimagnetic quantum critical point, in resemblance of that in the heavy fermion superconductors.

To summarize, we report optical investigations on the single crystal MnP and find that the optical conductivity can only be well understood with a multi-component Drude and Lorentz formula. In combination with band structure calculations, our analysis reveals the existence of two types of charge carriers with distinctly different characters. The short lifetime quasi-1D charge carriers become gapped in the helimagnetic phase and are primarily responsible for the magnetic properties, whereas the long lifetime charge carriers are more 3D-like and provide major contributions to the transport properties such as the dc conductivity. This puts a microscopic constraint for understanding the basic physics of MnP.

This work is supported by the 973 project of the Ministry of Science and Technology of China (Nos. 2015CB921300, 2015CB921303), the National Science Foundation of China (Nos. 11574358, 11522435), and the Strategic Priority Research Program of the Chinese Academy of Sciences (Grant No. XDB07020200).

P.Z., Y.J.X. and W.W. contributed equally to this work.

* pzheng@iphy.ac.cn
† yifeng@iphy.ac.cn

[1] W. Wu, J. G. Cheng, K. Matsubayashi, P. P. Kong, F. K. Lin, Ch. Q. Jin, N. L. Wang, Y. Uwatoko and J. L. Luo, Nature Commun. **5**, 5508 (2014).
[2] H. Kotegawa, S. Nakahara, H. Tou, and H. Sugawara, J. Phys. Soc. Jpn. **83**, 093702 (2014).
[3] J.-G. Cheng, K. Matsubayashi, W. Wu, J. P. Sun, F. K. Lin, J. L. Luo, and Y. Uwatoko, Phys. Rev. Lett. **114**, 117001(2015).
[4] Y. Sh. Wang, Y. J. Feng, J.-G. Cheng, W. Wu, J. L. Luo, and T. F. Rosenbaum, arXiv:1511.09152.
[5] M. Matsuda, F. Ye, S. E. Dissanayake, J.-G. Cheng, S. Chi, J. Ma, H. D. Zhou, J.-Q. Yan, S. Kasamatsu, O. Sugino, T. Kato, K. Matsubayashi, T. Okada, and Y. Uwatoko, Phys. Rev. B **93**, 100405(R) (2016).
[6] S. Yano, S. Itoh, T. Yokoo, S. Satoh, D. Kawana, Y. Kousaka, J. Akimitsu, and Y. Endoh, J. Magn. Magn. Mater. **33-38**, 347 (2013).
[7] S. Yano, J. Akimitsu, S. Itoh, T. Yokoo, S. Satoh, D. Kawana, and E. Yasuo, J. Phys.: Conf. Ser. **391**, 012113 (2012).
[8] R. Khasanov, A. Amato, P. Bonfà, Z. Guguchia, H. Luetkens, E. Morenzoni, R. De Renzi, and N. D. Zhigadlo, Phys. Rev. B **93**, 180509 (2016).
[9] G. Zh. Fan, B. Zhao, W. Wu, P. Zheng, and J. L. Luo, Sci. China Phys. Mech. Astron. **59**, 657403 (2016).
[10] A. Takase, and T. Kasuya, Phys. Soc. Jpn. **48**, 430 (1980).
[11] E. E. Huber, JR., and D. H. Ridgley, Phys. Rev. **135**, A1033 (1964).
[12] G. P. Felcher, J. Appl. Phys. **37**, 1056 (1966).
[13] T. Yamazaki, Y. Tabata, T. Waki, T. J. Sato, M. Matsuura, K. Ohoyama, M. Yokoyama, and H. Nakamura, J. Phys. Soc. Jpn. **83**, 054711 (2014).
[14] A. Zieba, M. Slota, and M. Kucharczyk, Phys. Rev. B **61**, 3435 (2000).
[15] Y. Todate, K. Yamada, Y. Endoh, and Y. Ishikawa, J. Phys. Soc. Jpn. **56**, 36 (1987).
[16] Y. Shiomi, S. Iguchi, and Y. Tokura, Phys. Rev. B **86**, 180404(R) (2012).
[17] M. S. Reis, R. M. Rubinger, N. A. Sobolev, M. A. Valente, K. Yamada, K. Sato, Y. Todate, A. Bouravleuv, P. J. von Ranke, and S. Gama, Phys. Rev. B **77**, 104439 (2008).
[18] S. Stolen, F. Gronvold, H. O. Haakonsen, J. T. Sipowska, and E. F. Westrum, Jr., J. Chem. Therm. **30**, 117 (1998).
[19] A. Takase, H. Yashima, and T. Kasuya, J. Phys. Soc. Jpn. **47**, 531 (1979).
[20] A. Yanase and A. Hasegawa, J. Phys. C: Solid State Phys.

13, 1989(1980).
[21] P. Bonfà, I. J. Onuorah, and R. De Renzi, arXiv:1603.08891 (2016).
[22] A. P. Grosvenor, S. D. Wik, R. G. Cavell, and A. Mar, Inorg. Chem. **44**, 8988 (2005).
[23] P. Blaha, K. Schwarz, G. K. H. Madsen, D. Kvasnicka, and J. Luitz, Wien2k: An Augmented Plane Wave plus Local orbital Program for Calculating the Crystal Properties (Technical University of Wien in Austria, ISBN39501031-1-2) (2001).
[24] R. Laskowski, G. K. H. Madsen, P. Blaha, and K.Schwarz, Phys. Rev. B **69**, 140408 (2004).
[25] Z. Gercsi and K. G. Sandeman, Phys. Rev. B **81**, 224426 (2010).
[26] A. Takase and T. Kasuya, J. Phys. Soc. Jpn. **47**, 491 (1979).